Materials Science & Engineering A 877 (2023) 145187

Contents lists available at ScienceDirect

Materials Science & Engineering A

journal homepage: www.elsevier.com/locate/msea

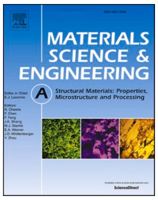

Effect of aging on secondary phases and properties of an S304H austenitic stainless steel

M. Tikhonova [a], A. Belyakov [a,*], R. Kaibyshev [a,b]

[a] Belgorod State University, Pobeda 85, Belgorod, 308015, Russia
[b] Russian State Agrarian University – Moscow Timiryazev Agricultural Academy, Moscow, 127550, Russia

ARTICLE INFO

Keywords:
Austenitic stainless steel
Aging
Precipitation
Mechanical properties
Corrosion resistance

ABSTRACT

Effect of aging up to 3000 h at 923 K on the microstructure, the secondary phases, the mechanical properties, and the intergranular corrosion was examined in an S304H-type austenitic stainless steel. The Cu-rich and NbC-type particles with sizes of 1.5 nm and 50 nm, respectively, were uniformly distributed throughout while$M_{23}C_6$-type carbides with a size of 40 nm precipitated mainly on the grain boundaries after aging for 100 h. Upon further aging a relatively fast coarsening of the boundary $M_{23}C_6$ carbides in accordance to a power law relationship with a particle growth exponent of 4 led to the formation of semi-continuous chains of these carbides along the grain boundaries. These chains diminished the fracture toughness; moreover, the steel became susceptible to intergranular corrosion. On the other hand, the uniform dispersions of NbC carbides and Cu-rich particles were less susceptible to coarsening under aging. The growth behavior of these particles could be expressed with a particle growth exponent of 3. A depletion of solid solution due to precipitate coarsening led to the ferrite appearance primarily along the austenite grain boundaries. The dispersion strengthening by carbide/nitride particles gradually decreased while that from Cu particles increased during annealing, resulting in the tension strength slightly increased with aging duration.

1. Introduction

Chromium-nickel austenitic stainless steels are widely used for critical components of modern fossil power plants, nuclear reactors, and petrochemical and chemical process plants owing to attractive combination of the yield strength and creep resistance at elevated temperatures along with reasonable corrosion and oxidation resistance [1–6]. Austenitic steels are able to withstand service temperatures ranging from 893 to 953 K and pressure loads ranging from 24 to 35 MPa [2–4]. Increasing temperature and allowable stress were attained by additional alloying [3,4]. Creep-resistant S304H steel was developed on the base of AISI304 steel for superheater and reheater tubes for ultra-supercritical pressure boilers [3,4]. The outstanding creep strength of S304H steels at high temperatures resulted from alloying by copper (3 wt%), niobium (0.4 wt%), boron (0.005 wt%), and increased to 0.08 wt% of nitrogen [3,4,7–9]. The strong carbide-forming elements such as Cr and Nb form $Cr_{23}C_6$ carbides and Nb(C, N) carbonitrides [7–9], whereas Cu-rich particles precipitate homogeneously [7–9].

The superior creep strength of S304H-type steels is attributed to high efficiency of the dispersion strengthening associated with coherent Cu particles and incoherent Nb(C,N) dispersoids. Stability of these particles against coarsening at elevated temperatures is a critical issue for long-term creep resistance of S304H-type steels [9–13]. Nb(C,N) carbonitrides exhibit superior dimensional stability despite large misfit implying incoherent interfaces of the dispersoids [8,13]. The primary Nb(C,N) particles with their dimensions ranging from 0.1 μm to 4 μm locate on the grain boundaries, whereas the secondary particles with a size of approx. 10 nm precipitate on dislocations during long-term aging or creep [8,13–18]. The fine Nb(C,N) and Cu particles give a significant contribution to the creep strength [17,19,20]. The Nb(C,N) carbonitrides may reportedly transform to Z-phase (CrNbN) particles under long-term aging [11,17,18], although the mechanical properties of the steel remained unaffected. The coarsening behavior of Cu particles is characterized by a grow exponent of 3 in accordance with the Lifshitz-Slyozov-Wagner theory [21,22]. After long-term aging for 50,000 h, the size of Cu particles may reach 40–80 nm depending on aging temperature of 650 °C–750 °C [23,24]. However, recent studies showed that the nano-sized Cu-rich precipitations can withstand against coarsening providing superior long-term creep strength [25–27]. The low interfacial energy of coherent Cu precipitates promotes their stability

---

* Corresponding author.
E-mail address: belyakov@bsu.edu.ru (A. Belyakov).

https://doi.org/10.1016/j.msea.2023.145187
Received 21 March 2023; Received in revised form 8 May 2023; Accepted 18 May 2023

[22]. Evolution of the uniformly dispersed Cu and Nb(C,N) particles during long-term aging affects tensile behavior of S304H-type steels insignificantly [11–15], although the dispersion strengthening deserves more accurate quantitative analysis. In contrast, the long-term aging diminished the impact toughness of S304H-type steels due to precipitation of $M_{23}C_6$ carbides and other phases on the grain boundaries [11,14,15], although this detrimental effect is not dramatic in S304H-type steels as compared to other alloys with higher Cr and Ni content [28–30].

The boundary particles play a role of nucleation sites for crack nucleation, and continuous chains of secondary phases on boundaries provide easy crack propagation path along the grain boundaries [28]. Transition from ductile transgranular fracture to brittle intergranular fracture substantially decreases the impact toughness after long-term aging [14,15,28–30]. The large portion of $M_{23}C_6$ carbides in austenitic stainless steels precipitate at grain boundaries [18,25,31]. Therefore, the impact toughness of S304H-type steels is significantly depend on the nucleation sites of $M_{23}C_6$ carbides and their ability to grow along the grain boundaries. In contrast to the Cu-rich phase, which quickly dissolves followed by the formation of chromium oxide protective layer [32], the large boundary carbides may lead to chromium depletion from austenite and, therefore, to intergranular corrosion [33–35]. Note here, the effect of aging on the susceptibility of S304H-type steels to intergranular corrosion is poorly known and has to be clarified.

Another important issue of the S304H-type steels is the stability of austenite during aging after redistribution of such strong austenite-stabilizing elements as Cu, N, and C. S304H-type steels consist of austenite and ferrite in an equilibrium state at temperatures below 1120 K [36] and precipitation of Cu-rich phase, carbides ($M_{23}C_6$), carbonitrides (Nb(C,N) and nitrides (Z-phase) may induce a partial transformation of austenite to ferrite. The formation of ferrite may lead to precipitation of boundary σ–phase particles and affect the performance of the steels [16]. The aim of the present study is to clarify the changes in the microstructure and the secondary phases during aging and to make clear the structure – property relationships in an S304-type austenitic stainless steel. In contrast to other studies on the aging behavior of austenitic stainless steels, the present paper is focused on the quantitative elaboration of the microstructure evolution including the particle dispersion that can be used to predict the change in the steel performance under exploitation conditions. In particular, the mechanisms of precipitate evolution including their coarsening behavior and the operating strengthening contributors are quantitatively assessed.

2. Experimental

An S304H-type austenitic stainless steel with a chemical composition of 0.10%C-18.2%Cr–7.85%Ni–3%Cu–0.50%Nb–0.008%B–0.12%N–0.95%Mn–0.10%Si and balance Fe (all in wt.%), was used as the starting material. The steel was subjected to solution treatment at 1373 K followed by air cooling. Then, the steel samples were aged for 100 h, 300 h, 1000 h, and 3000 h at 923 K.

The microstructural investigations were carried out using an FEI Technai-G2 transmission electron microscope (TEM) equipped with an EDAX energy dispersive X-ray analyzer and an FEI Nova Nano SEM 450 scanning electron microscope (SEM) equipped with an electron back-scatter diffraction (EBSD) analyzer incorporating an orientation imaging microscopy (OIM) system. The TEM specimens were grinded to about 0.1 mm in thickness. Then, the discs with a 3 mm diameter were cut and electropolished to perforation with a Tenupol-5 twinjet polishing unit using a 10% $HClO_4$ in CH_3COOH solution at 25 V. In addition, carbon extraction replicas were prepared for examination of dispersoids. More than 50 particles were analyzed using at least 5 typical TEM view-fields of appropriate magnification per each data point. The mean grain size was evaluated as an equivalent diameter of areas bounded by high-angle boundaries with misorientations of $\theta \geq 15^\circ$ using TSL OIM Analysis 6 software. The OIM images were subjected to clean-up procedures, setting a minimal confidence index of 0.1. The fracture surfaces of the mechanically tested samples and the surfaces after corrosion tests were examined using an FEI Quanta 200 3D SEM. The austenite/ferrite fraction was evaluated by magnetic induction method using an FMP30 Feritscope and by X-ray analysis using a Rigaku Ultima IV diffractometer. An equilibrium phase composition was calculated by ThermoCalc software with FE6 database.

The tensile specimens with a 25 mm gauge length and a 7 mm × 3 mm cross-section were tensioned at room temperature and 923 K at an initial strain rate of $1.3 \times 10^{-3}\ s^{-1}$ using an Instron universal testing machine (model 5082) equipped with a three-zone split furnace. The impact tests were performed at ambient temperature in accordance with ASTM E23-07 standard using an Instron IMP460 machine with an Instron Dynatup Impulse data acquisition system and V-notch (2 mm) impact specimens of $10 \times 10 \times 55\ mm^3$. The hardness was measured by Brinell tester with 5 mm ball indenter at room temperature. The corrosion properties were evaluated in accordance with ASTM G105-94 standard using a Potentiostat IPC-Pro. The impact and corrosion tests were carried out using one specimen for each condition provided that the property variations follow the common tendency.

3. Results

3.1. Microstructures and dispersed particles

The mean size of austenite grains (D_G) in the samples subjected to solution treatment is 7 μm. The particles of Nb(C,N) carbonitride with an average size of 100 nm are homogeneously distributed throughout the austenite grains. According to Thermo-Calc the volume fraction of these particles is about 0.05% at 1373 K.

The grain size, D_G, does not change during aging. The selected aging temperature is not high enough for recrystallization/grain growth resulting in any remarkable changes in the microstructure [37], which is moreover stabilized by precipitates. In contrast, a dispersion of secondary phase particles significantly depends on the aging duration (Table 1). Note here, the volume fractions in Table 1 were calculated by Thermo-Calc software. Aging results in precipitation of Cu-rich particles with their volume fraction of 0.8%. The coherent Cu dispersoids with an average size of 1.5 nm are observed after 100 h aging (Fig. 1). This particle size is close to a critical nucleation radius of Cu-rich particles of 1.15 nm estimated by Bai et al. [22]. The Cu particles exhibit cube-to-cube orientation relationship and their coherency is retained during aging because of similarity of lattice parameters of pure Cu (0.3615 nm) and austenite of S304H steel (0.3613 nm after solution treatment decreases to 0.3597 nm during aging [7,13,22]). The Cu

Table 1
Particle size (D) and volume fraction (F_V) of precipitates along with the hardness change of an S304H-type steel during aging at 923 K.

Aging time, h		Original	100	300	1000	3000
Nb(C,N)	D, nm	100 ± 15	50 ± 8	55 ± 8	70 ± 10	90 ± 13
	F_V, %	0.05	0.35	0.35	0.35	0.35
$M_{23}C_6$ (boundary)	D, nm	–	40 ± 7	70 ± 10	160 ± 25	200 ± 30
	F_V, %	–	1.6	1.6	1.6	1.6
$M_{23}C_6$ (interior)	D, nm	–	–	50 ± 8	50 ± 8	50 ± 8
	F_V, %	–	–	0.1	0.1	0.1
Cu	D, nm	–	1.5 ± 0.2	3 ± 0.5	4 ± 0.6	6 ± 0.9
	F_V, %	–	0.8	0.8	0.8	0.8
Hardness	HB	152 ± 5	179 ± 8	172 ± 8	175 ± 5	182 ± 8

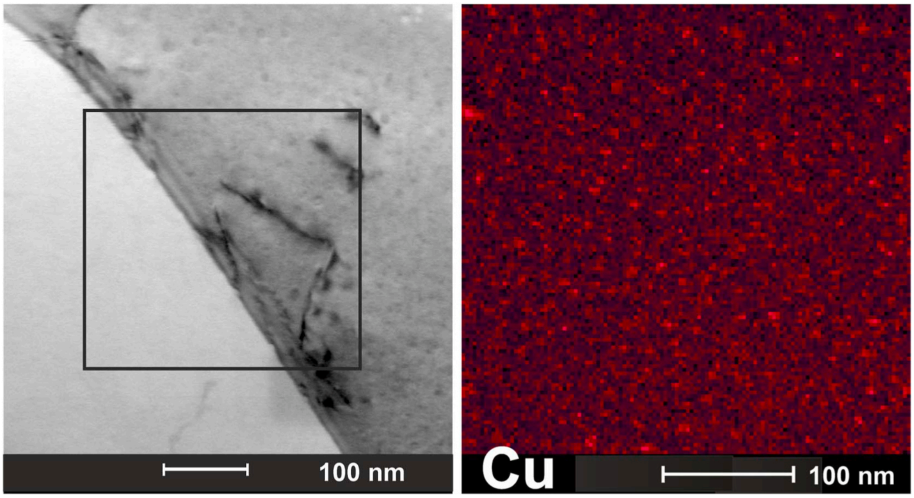

Fig. 1. Precipitation of Cu-rich phase in an S304H-type steel; STEM image and distribution of Cu within the indicated area after aging for 100 h at 923 K.

particles are highly susceptible to Ostwald repining under aging at 923 K in spite of coherency of their interfaces. A typical TEM image of the dispersed particles after 1000 h aging is shown in Fig. 2. The size of Cu particles increases to 4 nm during aging for 1000 h (Fig. 2) and then to 6 nm upon further aging for 3000 h (Table 1). Other uniformly distributed precipitations are Nb(C, N), the volume fraction of which counts 0.35% at 923 K and an average size is about 50 nm after 100 h aging (Fig. 3, Table 1). These finely dispersed Cu and Nb(C, N) particles are intended to enhance the creep resistance of an S304H-type steel upon a long-term service at elevated temperatures.

The precipitation of $M_{23}C_6$-type carbides with irregular shape and an average size of 40 nm readily appear at grain boundaries after 100 h aging (Fig. 3). These carbides comprise semi-continuous chains along grain boundaries. In addition, chromium readily segregates at the interface boundaries of large Nb(C, N) particles (Figs. 3 and 4), which serve as preferential nucleation sites for $M_{23}C_6$ precipitation. As a result, shells of $M_{23}C_6$ carbides appear on primary coarse Nb(C,N) carbontrides [9]. Aging is accompanied by the precipitation of $M_{23}C_6$ carbides in

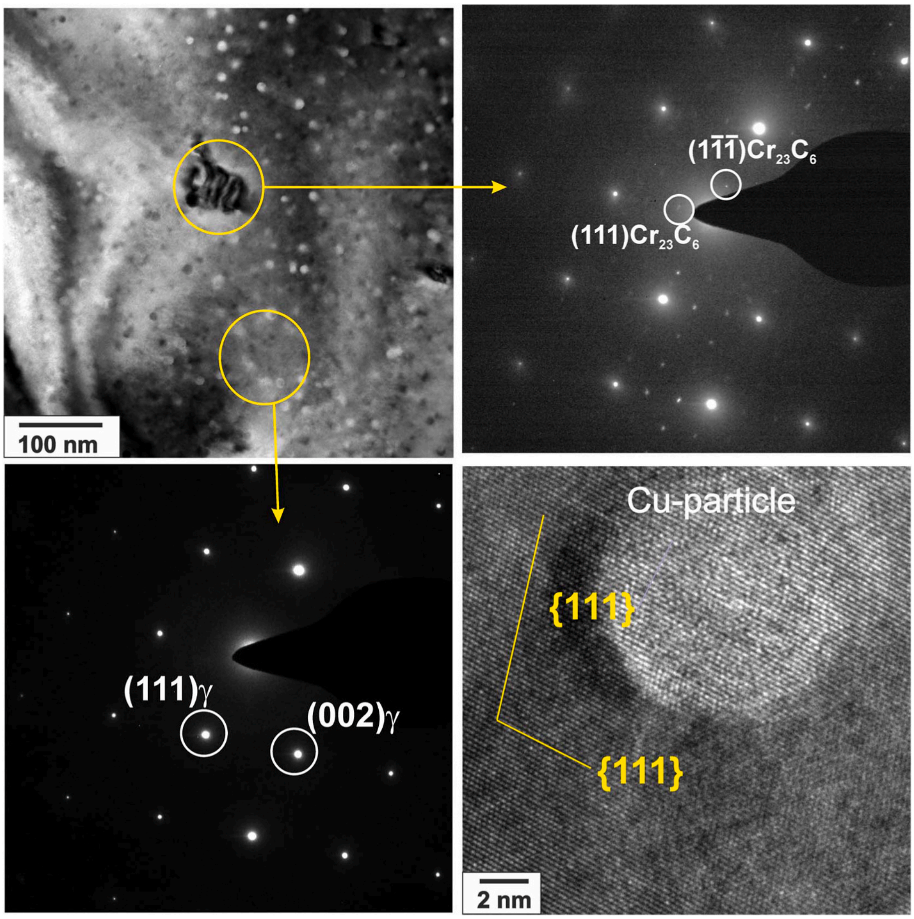

Fig. 2. TEM images showing $M_{23}C_6$ and Cu precipitates in an S304H-type steel after aging for 1000 h at 923 K.

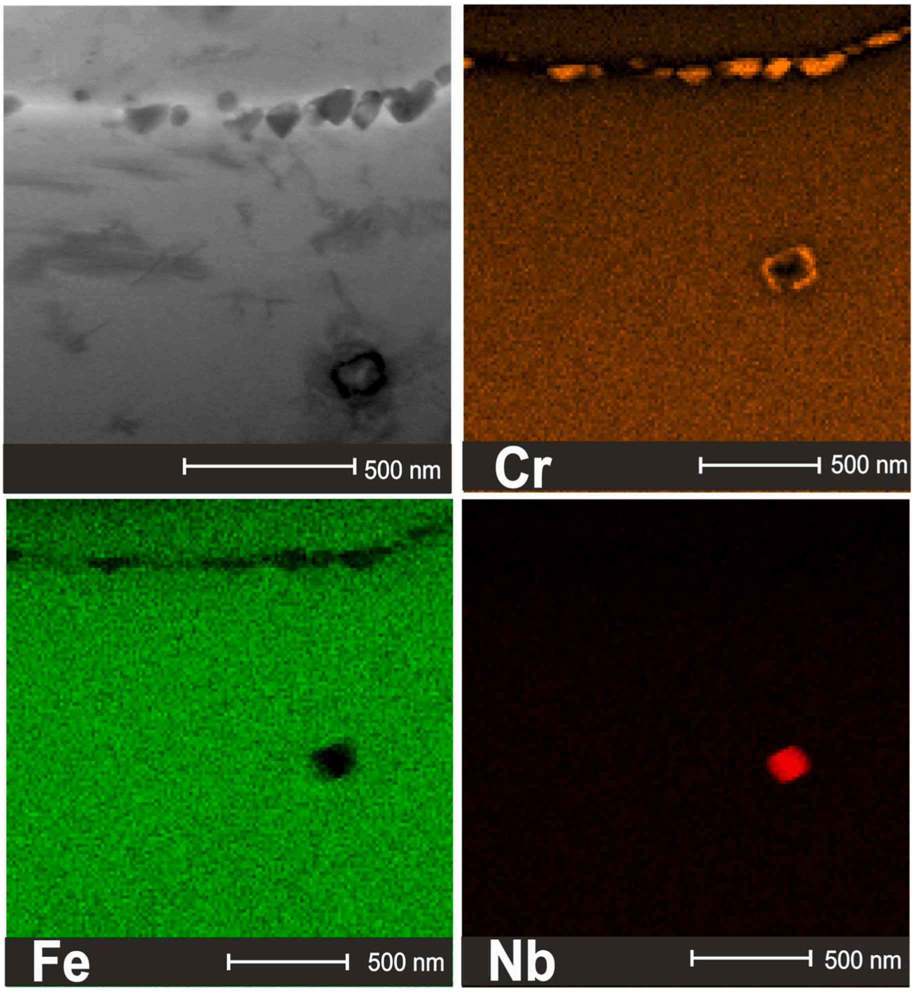

Fig. 3. STEM image and distribution of Cr, Fe, and Nb in an S304H-type steel after aging for 100 h at 923 K.

grain interiors and a growth of carbides located at the grain boundaries (Fig. 4, Table 1). Almost continuous chains of $M_{23}C_6$ carbides with rectangular shape appear along the boundaries. In contrast to relatively rapid coarsening of $M_{23}C_6$ carbides at the grain boundaries, the size of carbides located inside grains is almost independent on aging time (Table 1). The $M_{23}C_6$-type carbides precipitated inside the grains exhibit the following orientation relationship with austenite: $\{111\}_{M23C6} \parallel \{111\}_{\gamma\text{-Fe}}$ and $<110>_{M23C6} \parallel <110>_{\gamma\text{-Fe}}$ (Fig. 2) with a lattice misfit of $\Delta d = (d_{\gamma\text{-Fe}} - d_{M23C6})/d_{AVE} = 0.0146$ along $<111>$ (taking $d_{\{111\}\gamma\text{-Fe}} = 0.207$ nm and $d_{\{333\}M23C6} = 0.204$ nm [31,38]). Therefore, the stability of interior $M_{23}C_6$ carbides may be associated with the small lattice misfit in the direction normal to close-packed planes of {111}, resulting in a low-energy semi-coherent interface. In contrast, the boundary $M_{23}C_6$ carbides should exhibit incoherent interface with at least one neighboring grain. In addition, the grain boundary diffusion promotes their growth along boundary. Thus, the difference in coarsening behavior of $M_{23}C_6$ carbides located on boundaries and inside grain is attributed to the difference in their interfacial energy and diffusion path along grain boundaries. The precipitation of various numerous particles is accompanied by an increase in the hardness, which rapidly increases from 152 HB in the initial condition to an apparent saturation of approx. 180 HB after 100 h aging (Table 1).

An equilibrium volume fraction of ferrite is predicted by Thermo-Calc calculations as 16% at 923 K. Negligibly small amount of ferrite is registered after 100 h aging. Then, the volume fraction of ferrite gradually increases to about 8% after 3000 h (Fig. 5a). The ferrite appears primarily at boundaries of austenite grains, whereas the boundaries of annealing twins do not contribute to ferrite formation (Fig. 5b).

3.2. *Mechanical properties*

The engineering tensile stress-strain curves obtained at room temperature and 923 K for the steel samples aged up to 3000 h are shown in Fig. 6; and the values of yield strength ($\sigma_{0.2}$), ultimate tensile strength (UTS), and elongation-to-failure (δ) are listed in Table 2. All curves exhibit continuous yielding followed by pronounced strain hardening that results in a high ratio of UTS to $\sigma_{0.2}$. The aged samples are characterized by higher flow stresses at room temperature as compared to the steel after solution treatment (Fig. 6a). Remarkable increase in $\sigma_{0.2}$, the strain hardening, and UTS appear after aging for 100 h. Further aging insignificantly affects $\sigma_{0.2}$, while the work hardening rate and UTS increases. Note here that aging does not affect elongation-to-failure.

In contrast to the smooth stress-strain curves at room temperature, the serrated tensile flow curve is observed at 923 K (Fig. 6b). The largest serration amplitudes are observed in the initial state. This phenomenon is associated with the Portevin-Le Chatelier effect [39–41]. Type A serrations are distinguished as rises in the flow stress, followed by a drop to or below the general stress level are observed at all stress-strain curves. This type of serration associates with a repetitive continuous propagation of deformation bands of localized deformation. The serration amplitude decreases with aging duration. The sample aged for 1000 h can be characterized by an apparent smooth flow curves. The disappearance of serrations on the flow curve with increasing the aging time

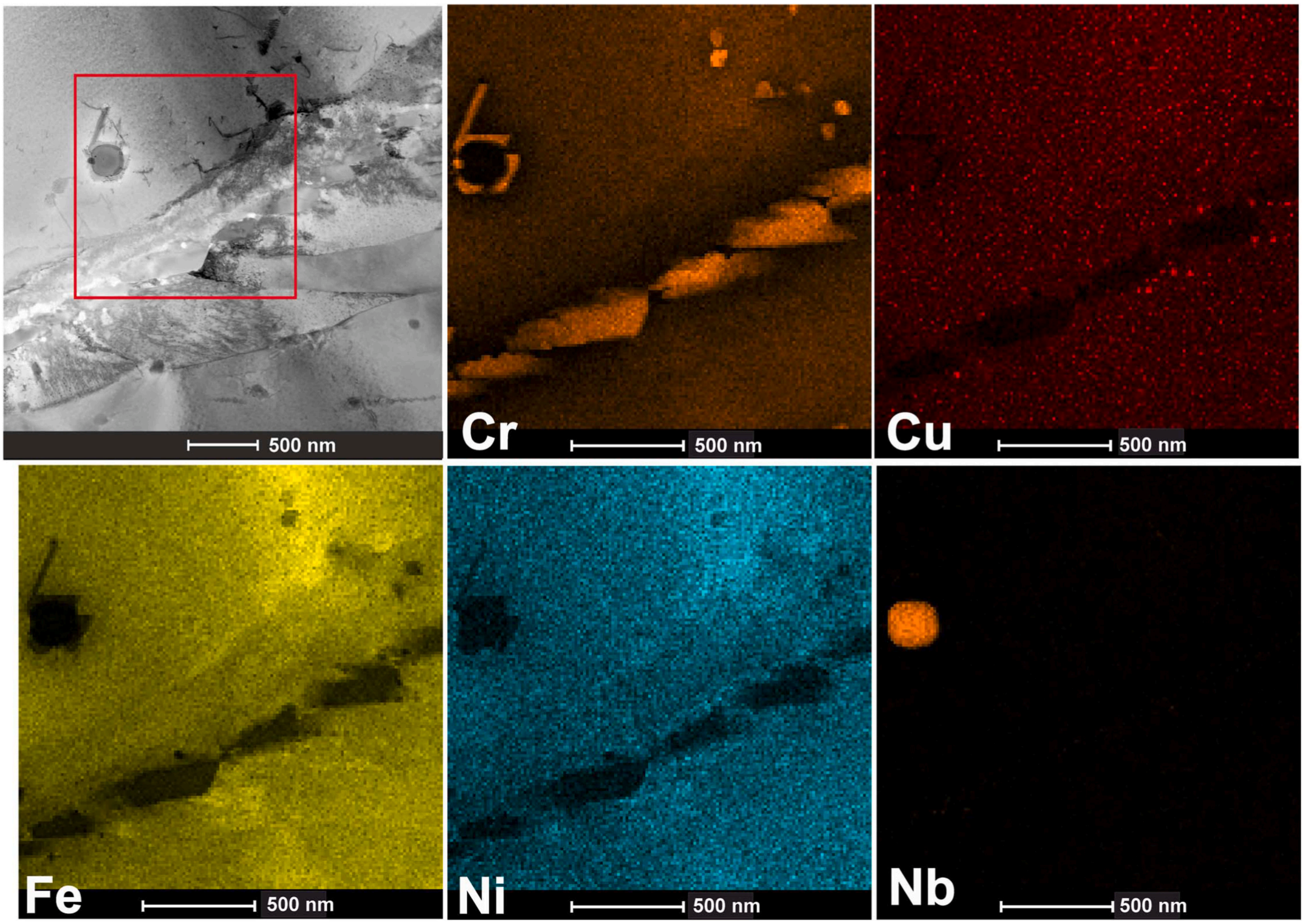

Fig. 4. STEM image and distribution of Cr, Cu, Fe, Ni, Nb in an S304H-type steel after aging for 1000 h at 923 K.

can be attributed to the depletion of substitutional and interstitial elements from austenite. Aging does not affect $\sigma_{0.2}$. In contrast, the strain hardening decreases remarkably, leading to a decrease in UTS. The most significant changes in the tensile behavior at 923 K are observed after 100 h aging, whereas the effect of further aging is negligibly small.

The load – displacement curves and the corresponding values of absorbed impact energy are presented in Figs. 7 and 8, respectively. Commonly, the specimens are characterized by almost the same shape of the impact load – displacement curves irrespective of aging duration (Fig. 7). Following the general yield (P_{GY}) the load increases to its maximum (P_M) followed by a gradual decrease [42,43]. Therefore, the fracture behavior is characterized by the stable crack propagation irrespective of aging time. The aging for 100 h increases the P_{GY} value that is indicative of the age-hardening, although further increase in the aging time does not lead to significant increase in P_{GY}. The P_M value is distinctly higher than the P_{GY} value that suggests high value of the fracture initiation energy [43]. The P_M value tends to decrease with increasing the duration of aging. The maximal load decreases slightly after aging for 300 h followed by remarkable decrease upon further aging. The displacement corresponding to P_M decreases from 6 to 4 mm after aging for 100 h and to 3 mm with an increase in the aging time to 3000 h. Thus, the main change in the load – displacement curves with an increase in the aging time is a decrease in the fracture initiation energy. The aging decreases the stress for the onset of the stable crack propagation. However, the fracture propagation energy remains almost unchanged.

A decrease in the fracture initiation energy results in a decrease of the absorbed impact energy (Fig. 8). The Charpy impact energy decreases from 170 to 130 J cm^{-2} just after 100 h aging followed by further decrease to 75 J cm^{-2} with an increase in aging time to 3000 h. An almost linear degradation of the impact toughness during aging in Fig. 7 suggests a logarithmic-type time relationship. In contrast to studies of Wang et al. [14] and Jin et al. [15], when the impact toughness exhibited quite weak dependence on long-term aging following a rapid decrease during 1000 h aging, the present steel is characterized by a gradual degradation of the impact toughness with an increase in the aging time that is associated with shortening the strain hardening stage during the impact loading.

3.3. Fractography

Typical SEM images of the fracture surfaces after the Charpy V-notch impact tests are shown in Fig. 9. It is seen that nucleation, growth and propagation of cracks occurs in ductile manner as suggested by dimple-type fracture surface. The primary Nb(C,N) particles may play a role of nucleation sites for microvoids in the sample after 100 h aging. These microvoids grow to a large size before coalescing. The smooth slip traces on the large walls of deep dimples in Fig. 9b–d are indicative of considerable plastic deformation before rupture [44]. Aging affects the depth and dimensions of dimples. Effect of aging for 3000 h on the fracture surface consists in significant decrease of dimple depth (Fig. 9f–h). The small dimple walls with a few slip trace suggest limited plastic deformation before fracture. The precipitation and coarsening of $M_{23}C_6$ carbides along the grain boundaries during aging facilitates the propagation of cracks. The dimple nucleation on the chains of boundary carbides advances the crack propagation without large preceding

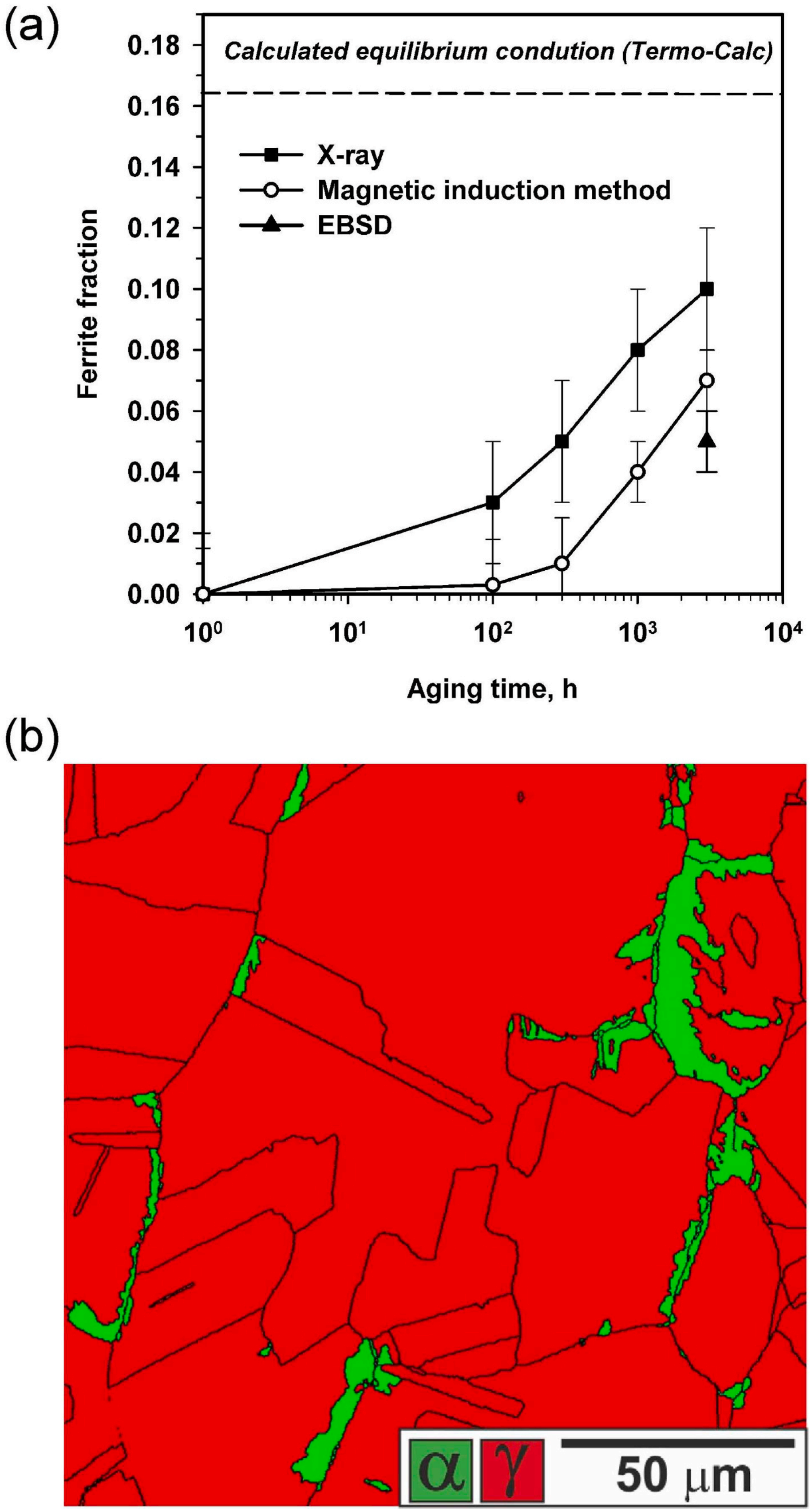

Fig. 5. Effect of aging time on ferrite fraction at 923 K (a) and the phase distribution in an S304H-type steel after aging for 3000 h (b).

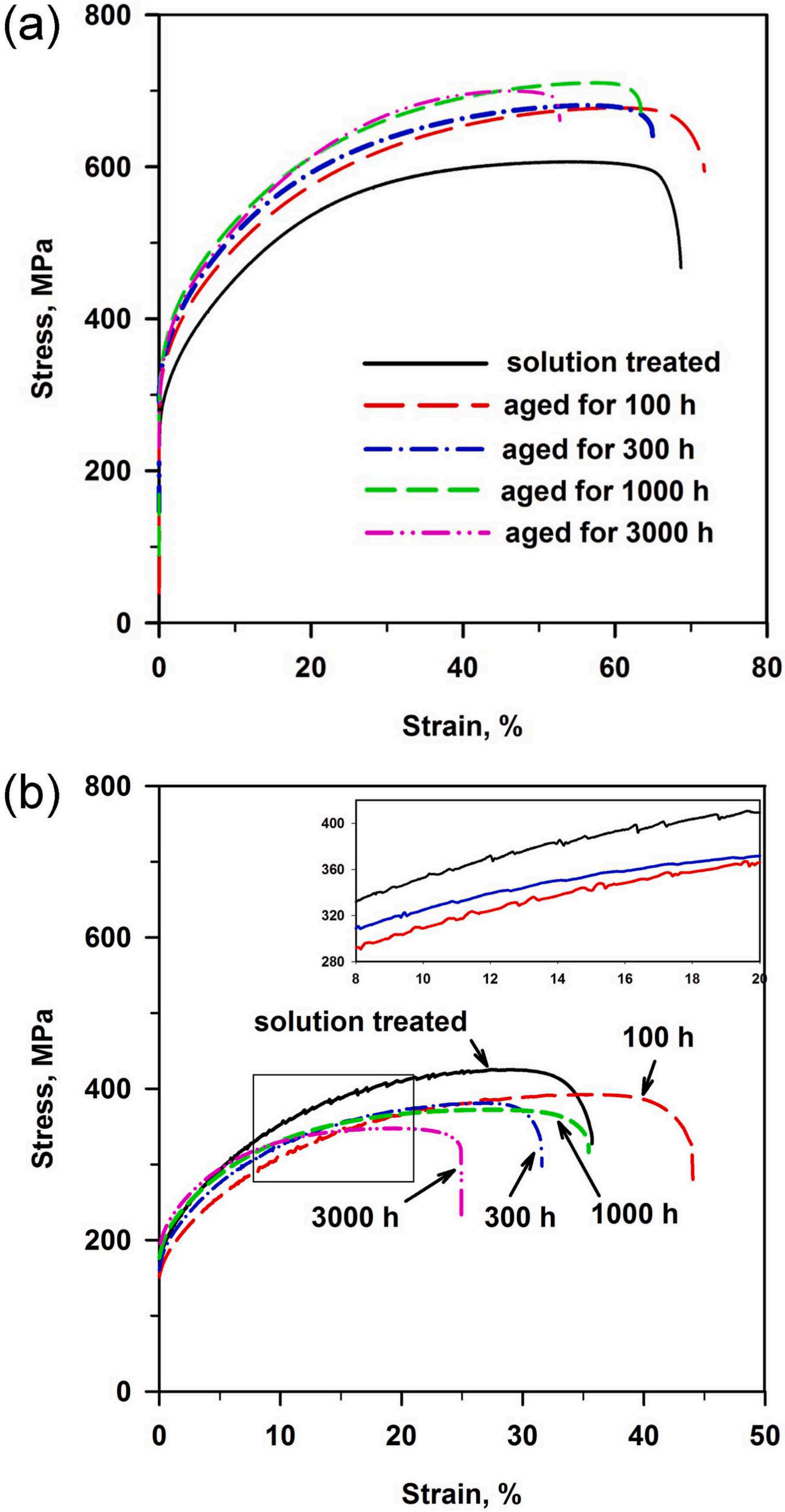

Fig. 6. Stress – strain curves obtained at a strain rate of 1.3×10^{-3} s^{-1} at room temperature (a) and 923 K (b) for S304H-type steel samples aged for 100–3000 h. Insert in (b) shows enlarged portions of flow curves with serrations.

Table 2
The yield strength ($\sigma_{0.2}$), the ultimate tensile strength (UTS), and elongation-to-failure (δ) at room temperature and 923 K of S304H-type steel samples aged for 100–3000 h at 923 K.

Aging time, h	$\sigma_{0.2}$ (MPa) at room temperature	UTS (MPa) at room temperature	δ (%) at room temperature	$\sigma_{0.2}$ (MPa) at 923 K	UTS (MPa) at 923 K	δ (%) at 923 K
0	280 ± 5	600 ± 10	70 ± 5	185 ± 10	420 ± 10	35 ± 5
100	305 ± 10	685 ± 15	70 ± 5	170 ± 20	365 ± 15	45 ± 5
300	325 ± 10	685 ± 15	65 ± 5	180 ± 15	380 ± 15	30 ± 5
1000	320 ± 10	710 ± 15	65 ± 5	195 ± 15	375 ± 15	35 ± 5
3000	310 ± 20	700 ± 25	55 ± 5	210 ± 20	350 ± 25	25 ± 3

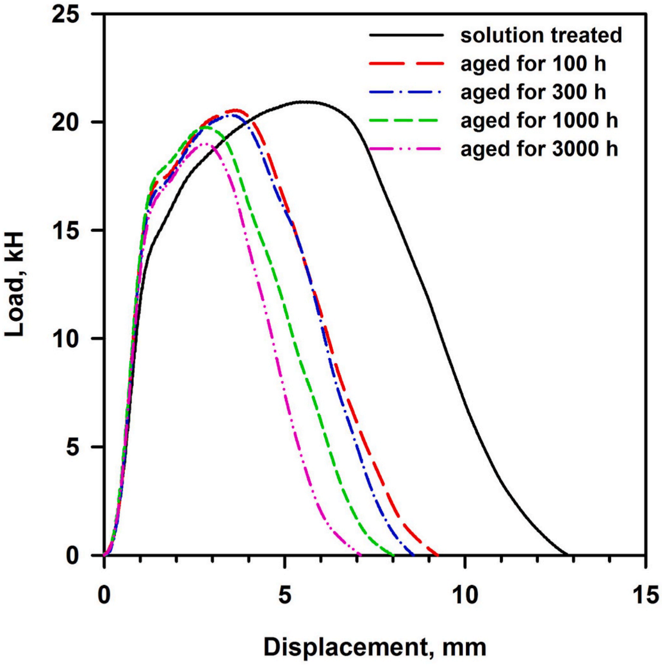

Fig. 7. Impact load – displacement curves obtained at room temperature for S304H-type steel samples subjected to aging at 923 K for different time.

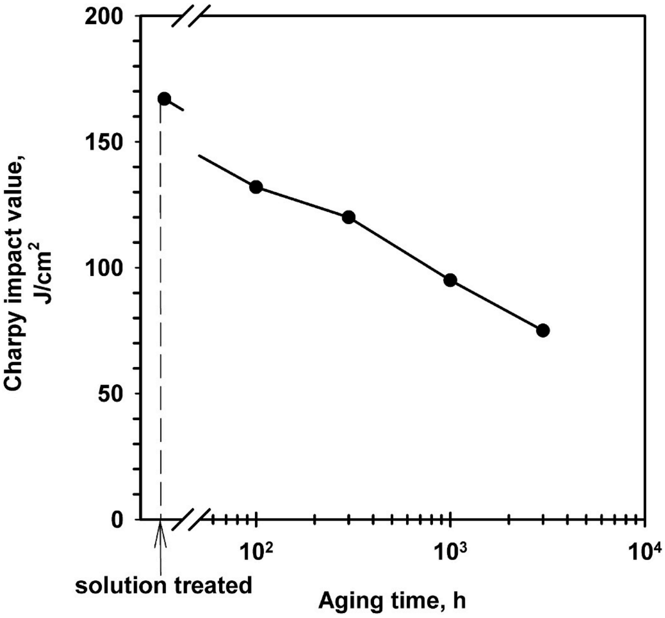

Fig. 8. V-notch impact absorbed energy at room temperature for S304H-type steel samples subjected to aging at 923 K for different time.

deformation, decreasing the impact toughness for the samples after aging. The large precipitate particles readily evolve at interphase boundaries [45,46]. Hence, the development of ferrite along the grain boundaries may also contribute to deteriorating the impact toughness.

3.4. Inter-granular corrosion

Fig. 10 shows the change in the reactivation/activation current ratio (Ir/Ia) with an increase in the aging time along with representative micrographs of corroded sample surfaces. A level of Ir/Ia = 0.11 separating the domains of fair and poor inter-granular corrosion resistances is also indicated. The initial solution treated steel sample is characterized by a good inter-granular corrosion resistance with a value of Ir/Ia well below the critical level. Aging with a duration of 100 h results in a dramatic degradation of the inter-granular corrosion resistance, i.e., the Ir/Ia value rises above 0.25. This drastic change in corrosion resistance resulted from the formation of Cr-rich $M_{23}C_6$ carbide chains on the grain boundaries and the formation of Cr-depleted zones adjacent to these boundary particles [35]. Further increase in the aging time is accompanied by an increase in the Ir/Ia ratio, which gradually approaches a saturation of about 0.7. The corresponding micrographs of the specimen surfaces after corrosion tests in Fig. 10 clearly show progressive degradation of intergranular corrosion resistance with an increase in aging time. Note in Fig. 10 that intergranular corrosion occurs at ordinary grain boundaries, whereas annealing twin boundaries remain unaffected. This suggests that carbide particles and corresponding Cr-depleted zones scarcely develop at twin boundaries. Thus, the formation of $M_{23}C_6$ carbide on the grain boundaries during aging highly increases the susceptibility of S304H steel to intergranular corrosion.

4. Discussion

4.1. Particle coarsening

Generally, the particle size can be related to aging time using an empiric power law expression with a growth exponent depending on the particle type and the aging conditions [47–49]. The particles of $M_{23}C_6$–type located at grain boundaries and the Cu-rich precipitations homogeneously distributed throughout the austenite grains exhibit apparently the most rapid coarsening in the present steel (Table 1). In contrast, the intragranular precipitates of Nb(C, N)–type and $M_{23}C_6$–type are characterized by a sluggish coarsening. The latter ones do not demonstrate any remarkable changes in their mean size, which remains at a level of 50 nm even after 3000 h aging. Such a high stability against coarsening for $M_{23}C_6$–type particles, which precipitate in grain interiors, can be attributed to their coherency with austenite matrix.

The rate of particle coarsening should depend on the coarsening mechanism. A power law-type relationship between the particle size and aging time with a size exponent of 3 is commonly held for the growth controlled by volume diffusion, i.e. $D^3 - D_0^3 = K_V t$, where D_0 and D are the initial particle size and that one at a time of t, and K_V is a numerical factor depending on volume diffusivity [50]. On the other hand, a size exponent of 4 has been suggested for the particle growth controlled by grain boundary diffusion, i.e. $D^4 - D_0^4 = K_B t$, where K_B is a factor depending on the grain boundary diffusivity [51]. Evidently, the

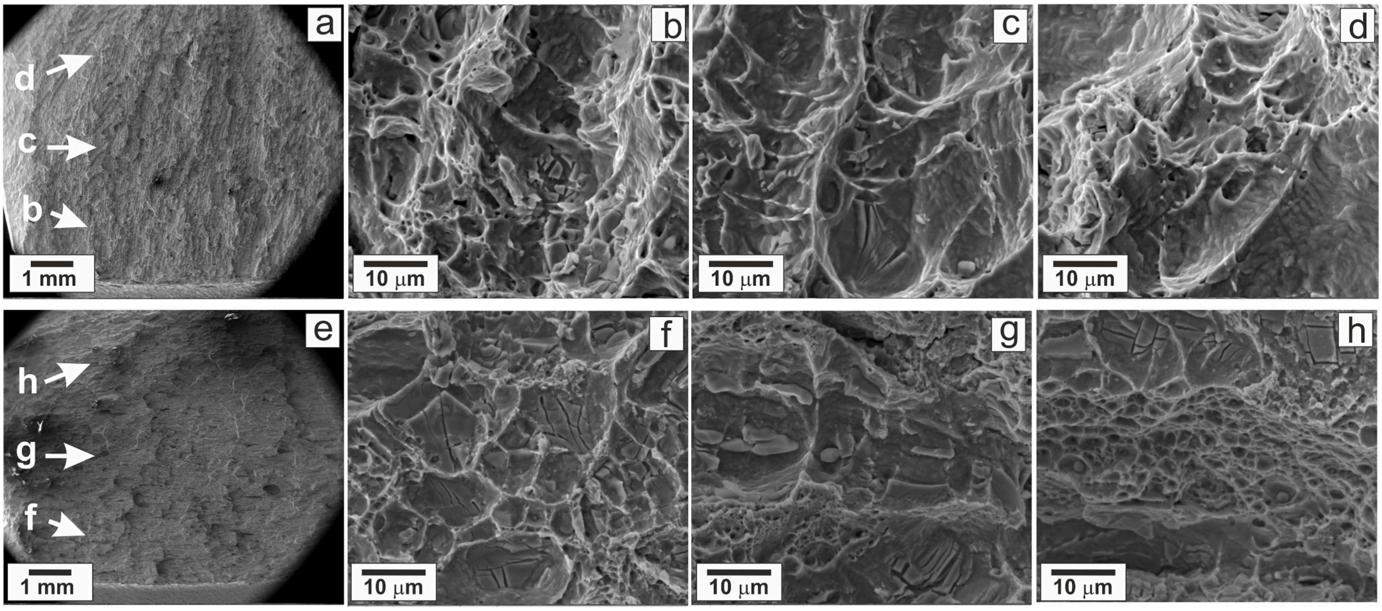

Fig. 9. SEM images of the fracture surfaces of S304H-type steel aged at 923 K for 100 h (a–d) and 3000 h (e–h).

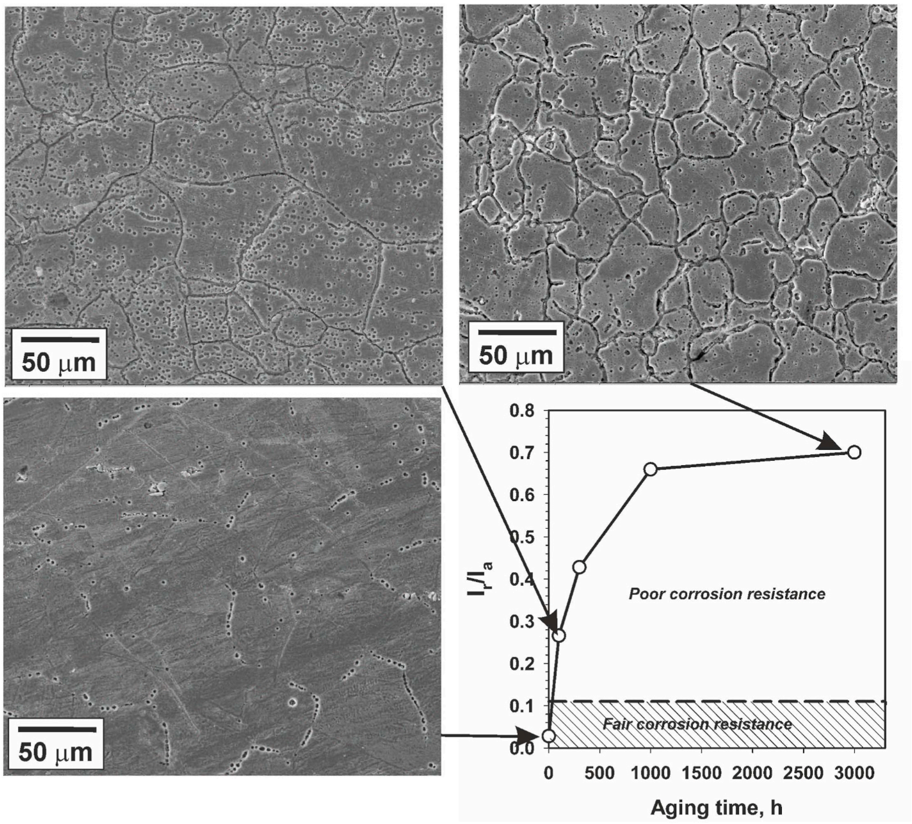

Fig. 10. SEM images of corrosion surfaces of original and aged at 923 K steel samples along with the degree of sensitization (Ir/Ia) vs aging time.

coarsening behavior of the Nb(C, N)-type and Cu-rich particles, which are homogeneously distributed in austenite grains, is controlled by volume diffusion and that of the $M_{23}C_6$–type particles located at grain boundaries is controlled by grain boundary diffusion. Taking D_0 as 50 nm, 20 nm and 1.5 nm for Nb(C, N), $M_{23}C_6$ and Cu particles, the respective relationships between the particle size and aging time are shown in Fig. 11, which validates the speculation about the coarsening mechanisms as described above. An apparent deviation of the coarsening kinetics of $M_{23}C_6$ at relatively short aging time from that extrapolated from the results obtained at long aging in accordance with the chosen coarsening mechanism can be caused by an additional effect of the particle growth by means of solid solution depletion. Indeed, the $M_{23}C_6$–type particles appear inside grains after 300 h aging; it means that $M_{23}C_6$ reaches its equilibrium volume fraction after rather long aging. Therefore, $M_{23}C_6$ gradually precipitates during relatively short aging, leading to the appearance of new particles concurrently with the

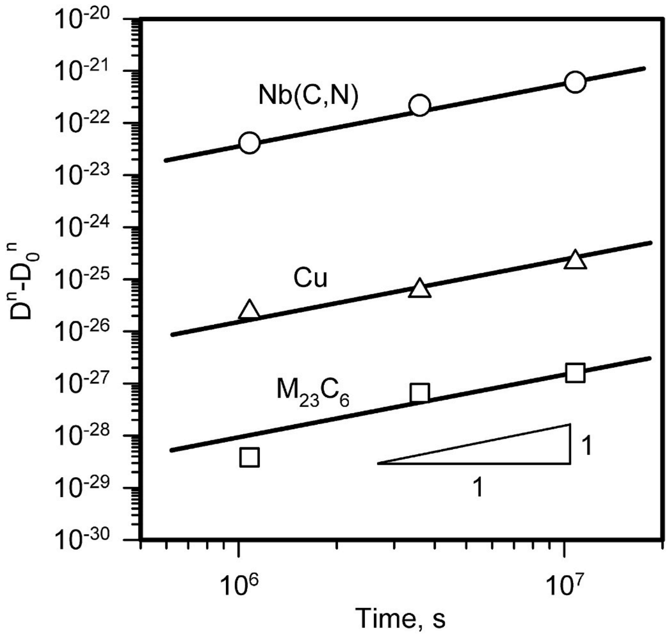

Fig. 11. Coarsening behavior of second-phase particles in an S304H-type steel during aging at 923 K.

growth of existing ones. Also, progressive degradation of inter-granular corrosion resistance, especially, after relatively short time annealing testifies to the growth of $M_{23}C_6$-type particles at grain boundaries owing to gradual depletion of solid solution.

4.2. Strengthening mechanisms

In spite of substantial changes in the phase content of the present steel during aging at 923 K, the strength of the aged samples does not vary significantly with aging time. The yield strength of the present steel can be expressed by a summation of individual strengthening mechanisms including solid solution strengthening, grain boundary (grain size) strengthening, and dispersed particle strengthening [52]. The solid solution strengthening including Peierls stress can be evaluated by the following empirical expression [53].

$$\sigma_{SS} = 65.5 + 496\,N + 356.5C + 20.1Si + 3.7Cr + 40.3Nb \tag{1}$$

Here, N, C, Si, Cr and Ni represent the corresponding chemical contents in wt%. The contribution from grain boundaries to overall strength can be expressed by the second term of Hall-Petch-type relationship [54,55].

$$\sigma_{GB} = k\,D_G^{-0.5} \tag{2}$$

Where k is a boundary strengthening factor, which has been reported as 120 MPa $\mu m^{0.5}$ at room temperature for annealed coarse grained austenitic steels [56]. The same value of k has been obtained for warm-to-hot rolled steel, taking into account dislocation strengthening as concurrent strengthening mechanism [57]. The change in k depending on the grain size domain, e.g., from 120 MPa $\mu m^{0.5}$–550 MPa $\mu m^{0.5}$ with a decrease in the grain size from 80 μm to 3 μm in a stainless steel [56], was probably affected by dislocation strengthening, whose contribution to overall strength reportedly increases with decreasing the grain size [58,59]. The grain boundary strengthening factor at 923 K is expected about a half of that at room temperature [60,61]. The particle dispersion strengthening depends on the interaction mechanism between dislocations and the particles. Homogeneously distributed particles of $M_{23}C_6$ and Nb(C, N) are overcome by Orowan bowing mechanism. Corresponding strengthening resulted from the dispersed particles with an average size of D and the particle spacing (edge to edge) of L can be estimated using the following relationship [52].

$$\sigma_{Or} = 0.4MGb\,\ln(0.82D/b)\,/\,(\pi L\sqrt{(1-\nu)}) \tag{3}$$

Where M is the Tailor factor, G is the shear modulus, b is the Burgers vector, and ν is the Poisson's ratio. The particle spacing is related to the particle volume fraction (F_V) as $L = 0.82d\,((0.5\pi/F_V)^{0.5}–1)$ [52]. The strengthening from the fine coherent Cu-rich particles is associated with difference in lattice parameters (a) resulting in lattice misfit strain, $\varepsilon = 0.67\,\Delta a/a$, as follows [52].

$$\sigma_{Coh} = 5.2\,M\,(G\varepsilon)^{1.5}\,(DF_V/Gb)^{0.5} \tag{4}$$

Then, the yield strength can be roughly evaluated as follows.

$$\sigma_{0.2} = \sigma_{SS} + \sigma_{GB} + \sigma_{Or}{}^{*} + \sigma_{Coh} \tag{5}$$

Where $\sigma_{Or}{}^{*} = (\sigma^2_{Or1} + \sigma^2_{Or2})^{0.5}$ represents the total strengthening from two kinds of dispersed particles [62], i.e., Nb(C, N) and $M_{23}C_6$.

Taking the grain boundary strengthening factors of 200 MPa $\mu m^{0.5}$ and 100 MPa $\mu m^{0.5}$, the yield strength of about 280 MPa and 180 MPa are calculated by Eqs. (1)–(5) for the present solution treated steel at room temperature and 923 K that agree well with the tensile tests (s. Fig. 6). Relatively high boundary strengthening factors in the present study could be associated with a large fraction of $M_{23}C_6$ particles precipitated at grain boundaries. The change in the yield strength and the strength contributions from solid solution, Cu particles (coherency strengthening), and uniformly distributed $M_{23}C_6$/Nb(C, N) particles (Orowan strengthening) as calculated by Eqs. (1)–(5) for room temperature and 923 K are shown in Fig. 12a and b, respectively. The results of calculation are in good agreement with the experimental measurements that prove the speculation above.

Therefore, the strength of the present S304H-type steel during aging is controlled by a specific variation of the contribution of different strengthening mechanisms. Namely, the solid solution strengthening quickly decreases during the aging because of the solid solution depletion. On the other hand, the dispersion strengthening increases during aging for 300 h owing to precipitation of various second phase particles. It is worth noting that the change in the dispersion strengthening due to particle coarsening upon further aging depends on the strengthening mechanisms. Gradual coarsening of uniformly distributed Nb(C, N) and $M_{23}C_6$ particles leads to a decrease in the Orowan strengthening, whereas coherency strengthening from growing Cu particles continuously increases much similar to other relevant studies [7,13,16]. The latter is very interesting phenomenon. That is an increase in the strength contribution with increasing the size of coherent particles that compensates a decrease in the strengthening from other growing dispersed particles. Hence, the change in the strengthening contributions from different mechanisms does not lead to significant change in the yield strength. A decrease in the solid solution strengthening is compensated by an increase in the dispersion strengthening. The latter provides gradual strengthening of such austenitic heat resistant steels under exploitation conditions, making them as a very attractive structural material for high temperature applications. Although, the over-aging effect after long-time exposure should be taken into account to predict the life-in-service of the steel components.

5. Conclusions

The aging behavior of an S304H-type stainless steels at 923 K was examined. The main results can be summarized as follows.

1. Aging was accompanied with precipitations and coarsening of various second-phase particles. Those included uniformly distributed Nb(C, N) carbonitrides with a size of 50 nm, $M_{23}C_6$-type carbides with a size of 40 nm, most of which located at grain boundaries, and tiny coherent Cu-rich particles with a size of 1.5 nm at an early stage of aging (after 100 h aging). Further aging for 3000 h increased the

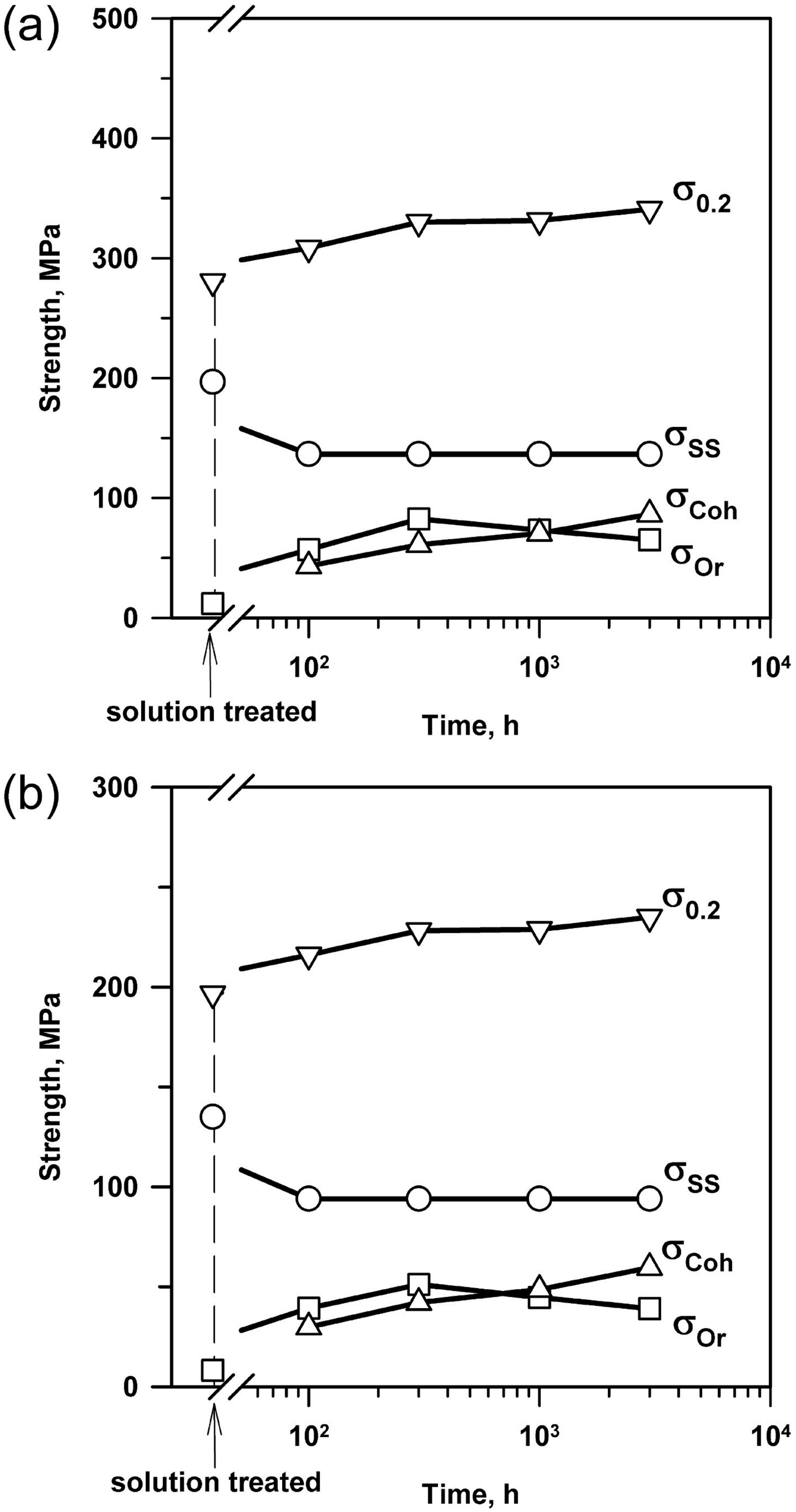

Fig. 12. The yield strength ($\sigma_{0.2}$) and the strength contributions from solid solution (σ_{SS}), Cu particles (σ_{Coh}), and $M_{23}C_6$/Nb(C, N) particles (σ_{Or}) uniformly distributed in an S304H-type steel subjected to aging at 923 K as calculated by Eqs. (1)–(5) for room temperature (a) and 923 K (b).

size of Cu, Nb(C, N), and $M_{23}C_6$ particles to 6 nm, 90 nm, and 200 nm, respectively.

2. The growth behavior of the second phase particles could be expressed by a power law functions depending on coarsening mechanism. The coarsening of Nb(C, N) and Cu particles located throughout the grains was controlled by volume diffusion with a particle growth exponent of 3. On the other hand, the growth of $M_{23}C_6$ particles located at grain boundaries was controlled by boundary diffusion with a particle growth exponent of 4.
3. The Thermo-Calc calculation predicted 16% of ferrite as equilibrium fraction at 923 K. Indeed, the aging behavior was characterized by a partial austenite to ferrite phase transformation, which readily occurred along the ordinary grain boundaries. The fraction of transformed ferrite comprised about 7% after 3000 h aging.
4. The development of rather large carbide particles at grain boundaries during aging affected the properties of the steel. The impact toughness gradually decreased with an increase in aging time, approaching KCV $= 75$ J cm^{-2} after 3000 h aging; and a rapid degradation of the inter-granular corrosion resistance occurred right after 100 h aging.
5. The strength of the steel did not change significantly during aging. The aging softening due to depletion of the solid solution at an early stage of aging was compensated by the precipitation strengthening. Then, the particle coarsening resulted in a decrease in the strengthening from Nb(C, N) and $M_{23}C_6$ particles by means of Orowan mechanism, whereas coherency strengthening progressively increased owing to growth of the Cu particles.

CRediT authorship contribution statement

M. Tikhonova: Investigation, Formal analysis, Writing – original draft. **A. Belyakov:** Methodology, Writing – review & editing. **R. Kaibyshev:** Conceptualization, Supervision.

Declaration of competing interest

The authors declare that they have no known competing financial interests or personal relationships that could have appeared to influence the work reported in this paper.

Data availability

Data will be made available on request.

Acknowledgements

Authors are grateful to the personal of the Joint Research Center, Technology and Materials, Belgorod State University for their assistance with instrumental analysis.

References

[1] K.H. Lo, C.H. Shek, J.K.L. Lai, Recent developments in stainless steels, Mater. Sci. Eng. R 65 (2009) 39–104, https://doi.org/10.1016/j.mser.2009.03.001.
[2] H. Wang, H. Du, Y. Wei, L. Hou, X. Liu, H. Wei, B. Liu, J. Jia, Precipitation and properties at elevated temperature in austenitic heat-resistant steels, Steel Res. Int. 92 (2021), 2000378, https://doi.org/10.1002/srin.202000378.
[3] F. Abe, T.-U. Kern, R. Viswanathan, Creep-resistant Steels, Woodhead Publishing, Cambridge, 2008.
[4] P. Barnard, Austenitic steel grades for boilers in ultra-supercritical power plants, in: A. Di Gianfrancesco (Ed.), Materials for Ultra-supercritical and Advanced Ultra-supercritical Power Plant, Woodhead Publishing, Cambridge, 2017, pp. 99–119, https://doi.org/10.1016/B978-0-08-100552-1.00003-8.
[5] K.L. Murty, I. Charit, Structural materials for Gen-IV nuclear reactors: challenges and opportunities, J. Nucl. Mater. 383 (2008) 189–195, https://doi.org/10.1016/j.jnucmat.2008.08.044.
[6] P.J. Maziasz, J.P. Shingledecker, N.D. Evans, M.J. Pollard, Developing new cast austenitic stainless steels with improved high-temperature creep resistance, J. Pressure Vessel Technol. 131 (2009), 051404, https://doi.org/10.1115/1.3141437.
[7] P. Ou, H. Xing, X.L. Wang, J. Sun, Tensile yield behavior and precipitation strengthening mechanism in Super304H steel, Mater. Sci. Eng. 600 (2014) 171–175, https://doi.org/10.1016/j.msea.2014.01.085.
[8] P. Ou, H. Xing, J. Sun, Precipitation of nanosized MX at coherent Cu-rich phases in Super304H austenitic steel, Metall. Mater. Trans. A 46A (2015) 1–5. https://doi:10.1007/s11661-014-2628-z.
[9] M.K. Dash, T. Karthikeyan, R. Mythili, V.D. Vijayanand, S. Saroja, Effect of long-term thermal exposures on microstructure and impression creep in 304HCu grade austenitic stainless steel, Metall. Mater. Trans. A 48A (2017) 4883–4894, https://doi.org/10.1007/s11661-017-4260-1.
[10] S. Tan, Z. Wang, S. Cheng, Z. Liu, J. Han, W. Fu, Effect of Cu content on aging precipitation behaviors of Cu-rich phase in Fe-Cr-Ni alloy, J. Iron Steel Res. Int. 17 (2010) 63–68, https://doi.org/10.1016/S1006-706X(10)60101-X.
[11] Y. Zhang, L. Zhu, A. Qi, Z. Lu, Microstructural evolution and the effect on mechanical properties of S30432 heat-resistant steel during aging at 650°C, ISIJ Int. 50 (2010) 596–600, https://doi.org/10.2355/isijinternational.50.596.
[12] I. Sen, E. Amankwah, N.S. Kumar, E. Fleury, K. Oh-ishi, K. Hono, U. Ramamurty, Microstructure and mechanical properties of annealed SUS 304H austenitic stainless steel with copper, Mater. Sci. Eng. 528 (2011) 4491–4499, https://doi.org/10.1016/j.msea.2011.02.019.
[13] P. Ou, H. Xing, X. Wang, J. Sun, Z. Cui, C. Yang, Coarsening and hardening behaviors of Cu-rich precipitates in Super304H austenitic steel, Metall. Mater. Trans. A 46A (2015) 3909–3916, https://doi.org/10.1007/s11661-015-3004-3.
[14] X. Wang, Y. Li, D. Chen, J. Sun, Precipitate evolution during the aging of Super304H steel and its influence on impact toughness, Mater. Sci. Eng. 754 (2019) 238–245, https://doi.org/10.1016/j.msea.2019.03.086.
[15] Xiao Jin, Xianxi Xia, Yuanfei Li, Yanfen Zhao, Fei Xue, Guodong Zhang, Quantitative study of microstructure evolution and the effect on mechanical properties of Super304H during aging, Mater. A. T. High. Temp. 36 (2019) 459–470, https://doi.org/10.1080/09603409.2019.1632508.
[16] Qingwen Zhou, Jiangwen Liu, Yan Gao, An insight into oversaturated deformation-induced sigma precipitation in Super304H austenitic stainless steel, Mater. Des. 181 (2019), 108056.
[17] V.T. Ha, W.S. Jung, Evolution of precipitate phases during long-term isothermal aging at 1083 K (810°C) in a new precipitation-strengthened heat-resistant austenitic stainless steel, Metall. Mater. Trans. A 43A (2012) 3366–3378, https://doi.org/10.1007/s11661-012-1150-4.
[18] G. Singh, Sung-Min Hong, K. Oh-ishi, K. Hono, E. Fleury, U. Ramamurty, Enhancing the high temperature plasticity of a Cu-containing austenitic stainless steel through grain boundary strengthening, Mater. Sci. Eng. 602 (2014) 77–88, https://doi.org/10.1016/j.msea.2014.02.054.
[19] M. Jiang, Y. Han, J. Sun, J. Sun, G. Zu, H. Chen, X. Ran, Precipitation of Cu- and Nb-rich phases and its strengthening effect in 17Cr ferritic stainless steel during high-temperature creep process, Mater. Char. 179 (2021), 111346, https://doi.org/10.1016/j.matchar.2021.111346.
[20] Yu Zhang, Hongyang Jing, Lianyong Xu, Lei Zhao, Yongdian Han, Yingxin Zhao, High-temperature deformation and fracture mechanisms of an advanced heat resistant Fe-Cr-Ni alloy, Mater. Sci. Eng. 686 (2017) 102–112, https://doi.org/10.1016/j.msea.2017.01.002.
[21] C. Chi, H. Yu, J. Dong, W. Liu, S. Cheng, Z. Liu, X. Xie, The precipitation strengthening behavior of Cu-rich phase in Ni contained advanced advanced Fe-Cr-Ni type austenitic heat resistant steel for USC power plant application, Prog. Nat. Sci. 22 (2012) 175–185, https://doi.org/10.1016/j.pnsc.2012.05.002.
[22] J.W. Bai, P.P. Liu, Y.M. Zhu, X.M. Li, C.Y. Chi, H.Y. Yu, X.S. Xie, Q. Zhan, Coherent precipitation of copper in Super304H austenite steel, Mater. Sci. Eng. 584 (2013) 57–62, https://doi.org/10.1016/j.msea.2013.06.082.
[23] A. Zielinski, R. Wersta, M. Sroka, Analysis of the precipitation process of secondary phases after long-term ageing of S304H steel, Bull. Pol. Acad. Sci. Tech. Sci. 69 (2021), e137520, https://doi.org/10.24425/bpasts.2021.137520.
[24] A. Zieliński, R. Wersta, M. Sroka, The study of the evolution of the microstructure and creep properties of Super 304H austenitic stainless steel after aging for up to 50,000 h, Arch. Civ. Mech. Eng. 22 (2022) 89, https://doi.org/10.1007/s43452-022-00408-6.
[25] Y. Li, X. Wang, Strengthening mechanisms and creep rupture behavior of advanced austenitic heat resistant steel SA-213 S31035 for A-USC power plants, Mater. Sci. Eng. 775 (2020), 138991, https://doi.org/10.1016/j.msea.2020.138991.
[26] R. Zhou, L. Zhu, Growth behavior and strengthening mechanism of Cu-rich particles in Sanicro 25 austenitic heat-resistant steel after aging at 973 K, Mater. Sci. Eng. 796 (2020), 139973, https://doi.org/10.1016/j.msea.2020.139973.
[27] T. Xi, M. Babar Shahzad, D. Xu, J. Zhao, C. Yang, M. Qi, K. Yang, Copper precipitation behavior and mechanical properties of Cu-bearing 316L austenitic stainless steel: a comprehensive cross-correlation study, Mater. Sci. Eng. 675 (2016) 243–252, https://doi.org/10.1016/j.msea.2016.08.058.
[28] Y. Li, X. Wang, Precipitation behavior in boundaries and its influence on impact toughness in 22Cr25Ni3W3CuCoNbN steel during short-term ageing, Mater. Sci. Eng. 809 (2021), 140924, https://doi.org/10.1016/j.msea.2021.140924.
[29] C.Z. Zhu, Y. Yuan, J.M. Bai, P. Zhang, J.B. Yan, C.Y. You, Y.F. Gu, Impact toughness of a modified HR3C austenitic steel after long-term thermal exposure at 650°C, Mater. Sci. Eng. 740–741 (2019) 71–81, https://doi.org/10.1016/j.msea.2018.10.084.
[30] Bicao Peng, Hongxiang Zhang, Jie Hong, Jiaqiang Gao, Qijiang Wang, Hanqian Zhang, Effect of aging on the impact toughness of 25Cr–20Ni–Nb–N steel, Mater. Sci. Eng. 527 (2010) 1957–1961, https://doi.org/10.1016/j.msea.2009.12.039.

[31] Zhen Zhang, Zhengfei Hu, Haoyun Tu, S. Schmauder, Gaoxiang Wu, Microstructure evolution in HR3C austenitic steel during long-term creep at 650°C, Mater. Sci. Eng. 681 (2017) 74–84, https://doi.org/10.1016/j.msea.2016.10.077.

[32] X.Y. San, B. Zhang, B. Wu, X.X. Wei, E.E. Oguzie, X.L. Ma, Investigating the effect of Cu-rich phase on the corrosion behavior of Super 304H austenitic stainless steel by TEM, Corrosion Sci. 130 (2018) 143–152, https://doi.org/10.1016/j.corsci.2017.11.001.

[33] K. Kaneko, T. Fukunaga, K. Yamada, N. Nakada, M. Kikuchi, Z. Saghi, J.S. Barnard, P.A. Midgley, Formation of M23C6-type precipitates and chromium-depleted zones in austenite stainless steel, Scripta Mater. 65 (2011) 509–512, https://doi.org/10.1016/j.scriptamat.2011.06.010.

[34] T. Sourmail, Precipitation in creep resistant austenitic stainless steels, Mater. Sci. Technol. 17 (2001) 1–14, https://doi.org/10.1179/026708301101508972.

[35] Guanshun Bai, Shanping Lu, Dianzhong Li, Yiyi Li, Intergranular corrosion behavior associated with delta-ferrite transformation of Ti-modified Super304H austenitic stainless steel, Corrosion Sci. 90 (2015) 347–358, https://doi.org/10.1016/j.corsci.2014.10.031.

[36] H. Tripathy, R. Subramanian, R.N. Hajra, A.K. Rai, M. Remgachari, S. Saibaba, T. Jayakumar, Calorimetric investigation of thermal stability of 304H Cu (Fe-17.7Cr-9.3Ni-2.95Cu-0.91Mn-0.58Nb-0.24Si-0.1C-0.12N-Wt Pct) austenitic stainless steel, Metall. Mater. Trans. 3E (2016) 234–249, https://doi.org/10.1007/s40553-016-0079-8.

[37] P. Dolzhenko, M. Tikhonova, M. Odnobokova, R. Kaibyshev, A. Belyakov, On grain boundary engineering for a 316L austenitic stainless steel, Metals 12 (2022) 2185, https://doi.org/10.3390/met12122185.

[38] M.H. Lewis, B. Hattersley, Precipitation of M23C6 in austenitic stainless steels, Acta Metall. 13 (1965) 1159–1168, https://doi.org/10.1016/0001-6160(65)90053-2.

[39] A.A. Mogucheva, I.A. Nikulin, R.O. Kaibyshev, V.N. Skorobogatykh, Portevin-Le Chatelier effect and causes of refractoriness of austenitic steel 08Kh18N8D3BR, Met. Sci. Heat Treat. 52 (2010) 128–134, https://doi.org/10.1007/s11041-010-9243-4.

[40] I. Nikulin, A. Kipelova, R. Kaibyshev, Effect of high-temperature exposure on the mechanical properties of 18Cr–8Ni–W–Nb–V–N stainless steel, Mater. Sci. Eng. 554 (2012) 61–66, https://doi.org/10.1016/j.msea.2012.06.011.

[41] A. Mogucheva, D. Yuzbekova, R. Kaibyshev, T. Lebedkina, M. Lebyodkin, Effect of grain refinement on jerky flow in an Al-Mg-Sc alloy, Metall. Mater. Trans. A 47 (2016) 2093–2106.

[42] H. Kuhn, D. Medlin, ASM Handbook. Volume 8: Mechanical Testing and Evaluation, tenth ed., ASM International, Mater. Park, USA,, 2000, p. 998.

[43] V. Dudko, A. Fedoseeva, R. Kaibyshev, Ductile-brittle transition in a 9% Cr heat-resistant steel, Mater. Sci. Eng. 682 (2017) 73–84, https://doi.org/10.1016/j.msea.2016.11.035.

[44] V. Kerlins, ASM Handbook. Volume 12: Fractography, ninth ed., ASM International, Mater., Park, USA, 1987, p. 857.

[45] A. Fedoseeva, I. Nikitin, N. Dudova, J. Hald, R. Kaibyshev, Effect of the thermo-mechanical processing on the impact toughness of a 12% Cr martensitic steel with Co, Cu, W, Mo and Ta doping, Metals 12 (2022) 3, https://doi.org/10.3390/met12010003.

[46] A. Fedoseeva, A. Dolzhenko, R. Kaibyshev, Thermo-mechanical processing as method decreasing delta-ferrite and improving the impact toughness of the novel 12% Cr steels with low N and high B contents, Materials 15 (2022) 8861, https://doi.org/10.3390/ma15248861.

[47] G. Wiener, Grain growth in high purity iron, Trans. ASM 44 (1952) 1169–1185.

[48] P. Hellman, M. Hillert, On the effect of second-phase particles on grain growth, Scand. J. Metall. 4 (1975) 211–219.

[49] F.J. Humphreys, M. Hatherly, Recrystallization and Related Annealing Phenomena, Pergamon Press, Oxford, 1996, pp. 235–325.

[50] M. Hillert, On the theory of normal and abnormal grain growth, Acta Metall. 13 (1965) 227–238, https://doi.org/10.1016/0001-6160(65)90200-2.

[51] A.J. Ardell, On the coarsening of grain boundary precipitates, Acta Metall. 20 (1972) 601–609, https://doi.org/10.1016/0001-6160(72)90015-6.

[52] T.J. Harrell, T.D. Topping, H. Wen, T. Hu, J.M. Schoenung, E.J. Lavernia, Microstructure and strengthening mechanisms in an ultrafine grained Al-Mg-Sc alloy produced by powder metallurgy, Metall. Mater. Trans. A 45A (2014) 6329–6343, https://doi.org/10.1007/s11661-014-2569-6.

[53] K.J. Irvine, T. Gladman, F.B. Pickering, The strength of austenitic stainless steels, J. Iron Steel Inst. 207 (1969) 1017–1028.

[54] E.O. Hall, The deformation and ageing of mild steel: II Characteristics of the Lüders deformation, Proc. Phys. Soc. B 64 (1951) 742–747, https://doi.org/10.1088/0370-1301/64/9/302.

[55] N. Petch, The cleavage strength of polycrystals, J. Iron Steel Inst. 174 (1953) 25–28.

[56] B.P. Kashyap, K. Tangri, On the Hall-Petch relationship in type 316L stainless steel at room temperature, Scripta Metall. 24 (1990) 1777–1782, https://doi.org/10.1016/0956-716X(90)90545-R.

[57] Z. Yanushkevich, A. Mogucheva, M. Tikhonova, A. Belyakov, R. Kaibyshev, Structural strengthening of an austenitic stainless steel subjected to warm-to-hot working, Mater. Char. 62 (2011) 432–437, https://doi.org/10.1016/j.matchar.2011.02.005.

[58] M. Tikhonova, V. Torganchuk, F. Brasche, D.A. Molodov, A. Belyakov, R. Kaibyshev, Effect of warm to hot rolling on microstructure, texture and mechanical properties of an advanced medium-Mn steel, Metall. Mater. Trans. A 50A (2019) 4245–4256, https://doi.org/10.1007/s11661-019-05340-8.

[59] P. Dolzhenko, M. Tikhonova, R. Kaibyshev, A. Belyakov, Dynamically recrystallized microstructures, textures, and tensile properties of a hot worked high-Mn steel, Metals 9 (2019) 30, https://doi.org/10.3390/met9010030.

[60] B.P. Kashyap, K. Tangri, On the Hall-Petch relationship and substructural evolution in type 316L stainless steel, Acta Metall. Mater. 43 (1995) 3971–3981. https://doi:10.1016/0956-7151(95)00110-H.

[61] Z. Yanushkevich, S.V. Dobatkin, A. Belyakov, R. Kaibyshev, Hall-Petch relationship for austenitic stainless steels processed by large strain warm rolling, Acta Mater. 136 (2017) 39–48, https://doi.org/10.1016/j.actamat.2017.06.060.

[62] T.J. Koppenaal, D. Kuhlmann-Wilsdorf, The effect of prestressing on the strength of neutron-irradiated copper single crystals, Appl. Phys. Lett. 4 (1964) 59–61, https://doi.org/10.1063/1.1753962.